Direct growth of 2D nickel hydroxide nanosheets intercalated with polyoxovanadate anions as a binder-free supercapacitor electrode

Jayavant L. Gunjakar, Akbar I. Inamdar, Bo Hou, SeungNam Cha, S. M. Pawar, Abu Talha A. A., Harish S. Chavan, Jongmin Kim, Sangeun Cho, Seongwoo Lee, Yongcheol Jo, Hyungsang Kim and Hyunsik Im

Division of Physics and Semiconductor Science, Dongguk University, Seoul 04620, South Korea

Department of Engineering Science, University of Oxford, Parks Road, OX1 3PJ, UK

TOC graphic

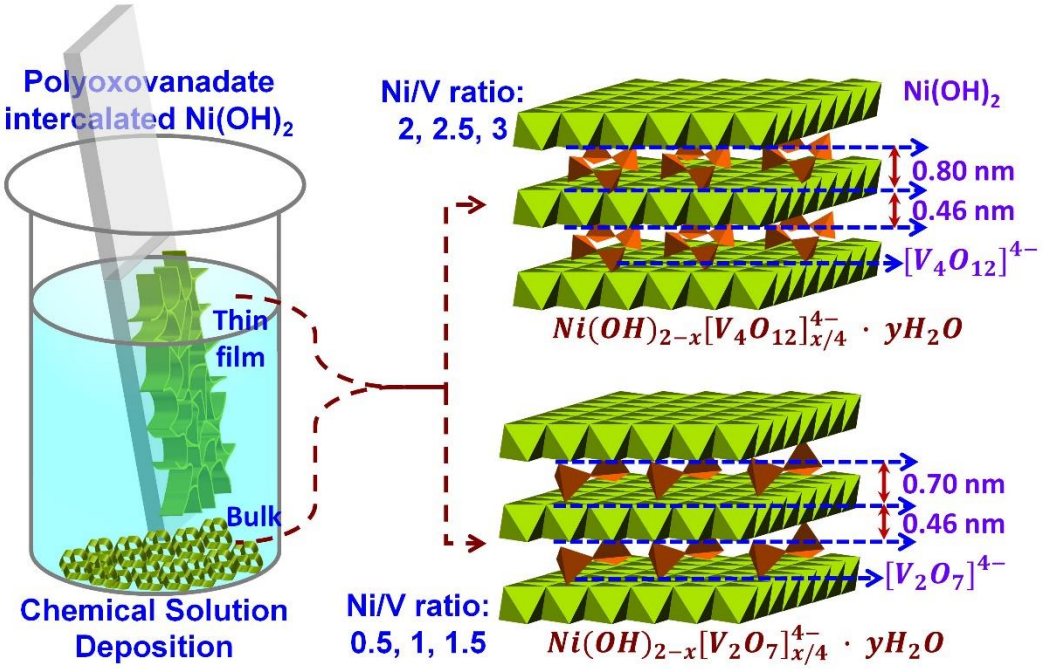

ABSTRACT

A mesoporous nanoplate network of two-dimensional (2D) layered nickel hydroxide $Ni(OH)_2$ intercalated with zero-dimensional (0D) polyoxovanadate ($Ni(OH)_2$−POV) was built using a chemical solution deposition method. This approach will provide high flexibility in controlling the chemical composition and the pore structure of the resulting $Ni(OH)_2$−POV nanohybrids. The layer-by-layer ordered growth of the $Ni(OH)_2$ −POV is demonstrated by powder X-ray diffraction and cross-sectional high-resolution transmission electron microscopy. The random growth of the intercalated $Ni(OH)_2$−POV nanohybrids leads to the formation of an interconnected network morphology with a highly porous stacking structure whose porosity is controlled by changing the ratio of $Ni(OH)_2$ and POV. The lateral size and thickness of the $Ni(OH)_2$−POV nanoplates are ~ 400 nm and from ~ 5 nm to 7 nm, respectively. The obtained thin films are highly active electrochemical capacitor electrodes with a maximum specific capacity of 1440 Fg^{-1} at a current density of 1 mA/g, and they withstand up to 2000 cycles with an excellent capacity retention of 85%. The superior electrochemical performance of the $Ni(OH)_2$−POV nanohybrids is attributed to the expanded mesoporous surface area and the intercalation of the 0D POV. The experimental findings highlight the outstanding electrochemical functionality of the 2D $Ni(OH)_2$−POV nanoplate network that will provide a facile route for the synthesis of low-dimensional hybrid nanomaterials for highly-active electrochemical electrode applications.

INTRODUCTION

One of the key challenges in thin film technology is integrating novel complex material architectures with tailored and emergent properties into functional devices. The ultimate properties of such complex materials with thin-film structures are not easy to predict due to their structural and electronic complexity. The deposition of such systems, with the requirements regarding the complex structure, uniformity, crystallinity and homogeneity of their compositions as well as the requisite extreme control over the thickness, is difficult to monitor over a large area with the use of the existing physical/chemical vapour deposition (CVD) methods.[1, 2]

The rapid depletion of fossil fuels, the growing environmental pollution, and global warming are central threats to the sustainable development of human beings. Due to the anticipated energy crisis, novel methods for the attainment of alternative and renewable energies are under investigation. Particularly, the fabrication of highly efficient and environmentally friendly energy storage systems are highly desirable.[3, 4] The electrochemical capacitor that is popularly known as the "supercapacitor" is a very attractive energy-storage device due to its high specific power (> 10 kW kg^{-1}) and excellent cycle life with a moderate specific energy (~10 Wh kg^{-1}).[5,6] The functionality of supercapacitors is based on the charge-storage mechanism of ion adsorption (electrochemical double layer capacitors, EDLCs) or surface redox reactions (pseudocapacitors).[7] Taking into account the fact that EDLCs can store an electrical charge near the electrode surface through the ion adsorption mechanism and the redox reactions of the surface species (pseudocapacitors), high-surface-area low-dimensional transition metal oxides (TMOs), hydroxides, and conducting polymers are promising candidates for electrochemical capacitors.[8-11] Several layered TMO and hydroxide nanostructures have received special attention because of their use in applications like photocatalysts, electrodes, electrocatalysts, gas adsorbents, and drug

delivery vectors, among others.[12-16] Among many of the layered materials, layered double hydroxide (LDH) materials with the general formula $[M^{2+}_{1-x}\ M^{3+}_{x}(OH)_2]^{x+}[A^{n-}_{\ x/n}]^{x-}\cdot mH_2O$, in which M^{2+}, M^{3+}, and A^{n-} are the suitable divalent metal ions, trivalent metal ions, and charge-balancing anions, respectively, have garnered special attention as a pseudocapacitive electrode material with very high specific capacitances owing to their diverse chemical composition, which makes it easier to tune their specific capacitances by varying the type and concentration of the redoxable transition metal ions.[10, 17] Moreover, the LDHs crystallize in a sheet-like morphology composed of diverse transition metal ions that are stabilized in the octahedral sites of an LDH lattice, and their accessibility in the hydrated gallery space between the hydroxide layers affords the accumulation of significant charge amounts at the expanded surface through the electrical double layer and the Faradaic (redox) process of the surface species.[18,19]

In recent years, extensive research has been devoted to the study of a particular class of LDH compounds for which x =0 and that consists of a single type of metal cation. The cation is formed by the stacking of positively charged hydroxyl-deficient layers, which are represented by the general formula $[M^{2+}(OH)_{2-x}A^{n-}_{x/n}\ yH_2O]$, where x = 0.2 - 0.4; M = Ni, Co, Zn, and Mg; A^{n-} = Cl^-, NO_3^-, SO_4^{2-}, and CO_3^{2-}; and y = 0.6 - 1.[20-22] Initially, efforts were directed toward deposition of LDH thin films from their bulk counterpart, which leads to an aggregation of the powdery translucent LDHs with many cracks. The cracks are due to surface strains that originate from the substrate surface, which does not adhere well to the substrate.[23,24] High electrostatic attraction between the positively charged LDH nanosheets and the charge-balancing anions with a high charge-to-size ratio are incorporated into the LDH interlayer gallery space, thereby creating LDH materials that suffer from a limited accessibility regarding their inter-gallery space and functionality.[25] To circumvent this drawback, several attempts were made to synthesize LDH

crystals with an expanded gallery space and with the incorporation of bulky inorganic anions to hybridize the LDH crystals with various guest species, such as inorganic, organic, polymeric, and biomolecules/nanostructures.[12,13,26-30]

Here we fabricated a nanoplate network of 2D layered $Ni(OH)_2$ that is intercalated with 0D polyoxovanadate ($Ni(OH)_2$−POV) using a simple and efficient chemical solution deposition (CSD) technique. The intercalation of the 0D polyoxovanadate into the 2D $Ni(OH)_2$ remarkably improves the ionic conductivity and diffusion, which results in a superior electrochemical energy-storage performance. Our study elucidates the intercalation effects on the electrochemical activity and stability of the $Ni(OH)_2$−POV based electrodes. The optimised $Ni(OH)_2$−POV electrode exhibited a high specific capacitance of 1440 F/g at a scan rate of 50 mV/s and an excellent cycling performance over 2000 cycles with a capacity retention of 85%.

Results and Discussion

Film Formation and Reaction Mechanism

The CSD of thin films is a controlled precipitation technique that is based on the principle of the solid-phase formation during the transformation from a supersaturated to a saturated state.[31] For the synthesis of the $Ni(OH)_2$−POV nanosheet thin films, a supersaturated aqueous solution of a hexamine $Ni(NH_3)_4^{+2}$ complex, and sodium orthovanadate ($Na_3VO_4^-$) is transformed to the saturated state via the gradual evaporation of ammonia (NH_3). The CSD bath is kept at a constant temperature of 50 ºC. The dissolution of the $NiCl_2$ in water initially facilitates the emergence of an octahedral hexa-aqua nickel (II) complex ion, as follows:[32]

$$x\mathrm{NiCl_2} + xy\mathrm{H_2O} \rightarrow x[\mathrm{Ni(H_2O)}_y]^{2+}_{(aq)} + 2x(\mathrm{Cl_2})^- \quad (1)$$

During the addition of the liquid NH_3, a greenish precipitate of hydrated $Ni(OH)_2$ is formed according to the hydroxide-group-derived '*olation*' process of the stepwise replacement of the H_2O ligand molecules, as follows:

$$x[\mathrm{Ni(H_2O)}_p]^{2+} + y(OH)^{2-} \leftrightarrow [\mathrm{Ni}_x(\mathrm{OH})_y(\mathrm{H_2O})_{xp-y}]^{(2x-y)+} \text{ at pH} < 9$$

and

$$x[\mathrm{Ni(H_2O)}_p]^{2+} + y(OH)^{2-} \leftrightarrow \mathrm{Ni}_x(\mathrm{OH})_{2n}\,(s) + (xp-y)H^{+} \text{ at pH} > 9 \qquad (2)$$

Upon the further addition of excess NH_3 solution, the green precipitate of the $Ni(OH)_2$ is transformed into a clear blue solution of the hexammine nickel complex ($Ni(NH_3)_q^{2+}$), where q is the coordination number with the most stable value of 6 for the Ni^{2+}.[33, 34] The formation of the hexammine nickel complex prevents a spontaneous precipitation, which leads to the formation of a supersaturated solution, as follows:

$$\mathrm{Ni_x(OH)_{2x}} + \mathrm{qNH_4^+} + \mathrm{q(OH)^-} \leftrightarrow \mathrm{Ni_x\,(NH_3)_q^{2x+}} + \mathrm{qH_2O} + \mathrm{2x(OH)^-} \text{ at pH} > 12 \qquad (3)$$

The aqueous solution of the vanadium precursor produces a large variety of isopolyvanadate species that exhibit diverse structures ranging from chain metavanadates $[VO_3^-]_n$ to layered oxides $[V_2O_5]$ and compact polyanions $[V_{10}O_{28}]^{6-}$. The structural nature of these species is highly dependent on the concentration and pH.[35, 36] The V^{5+} ions induce the $[V(OH_2)_6]^{5+}$ solvated species that are formed in the aqueous solution and are surrounded by dipolar H_2O molecules.

Since the V^{5+} and H_2O possess a strong polarizing power and Lewis properties, respectively, some of the electrons can be transferred from the $3a_1$ orbital of the water molecule to the empty 3d orbitals of the V^{5+}. The resultant spontaneous acidification and deprotonation of the H_2O molecules are represented by the following hydrolysis reaction:

$$[\mathrm{V(OH_2)_6}]^{5+} + h\mathrm{H_2O} \rightarrow [\mathrm{V(OH)}_h(\mathrm{OH_2})_{6-h}]^{(5-h)+} + h\mathrm{H_3O^+} \qquad (4)$$

where the hydrolysis ratio *h* increases with the pH leading to the formation of aquo, hydroxo, or oxo species. Initially, the pH of the Na_3VO_4 solution is close to ~ 12, producing a monomeric tetrahedral-vanadate oxo-anionic VO_4^{3-} species in which four equivalent oxygen atoms surround the V-V. A $Ni(OH)_2$–POV CSD bath is formed by the addition of a monomeric-orthovanadate VO_4^{3-} solution to a supersaturated solution of the hexammine nickel complex. The addition of the above solution creates a transparent supersaturated CSD bath with a slight increase in the pH depending on the amount of the VO_4^{3-} precursor and a colour change from ~~a~~ transparent blue to ~~a~~ dark cyan. The CSD bath is maintained at an elevated temperature (~ 50 ºC) along with the vertically immersed substrates; consequently, the ionic product exceeds the solubility product through its release of the H_2O and NH_3. The CSD bath gradually becomes saturated, and precipitation occurs through the heterogeneous growth of the α-$Ni(OH)_2$, which is pillared with the polyoxovanadate species on the substrate, as well as the homogeneous growth in the solution phase.

The type of intercalated species can be predicted by observing the change of the pH. As the precipitation process proceeds, the pH changes from 12.5 to ~ 7. As the pH drops gradually to ~ 9, condensation occurs due to a continuous deprotonation that leads to the transformation of the VO_4^{3-} species to dimeric pyrovanadates $[V_2O_7]^{4-}$. In the pH span from 7 to 9, a more condensed cyclic-metavanadate $[V_4O_{12}]^{4-}$ can be formed;[36] consequently, the intercalated polyoxovanadium species are most likely to be either $[V_2O_7]^{4-}$ or $[V_4O_{12}]^{4-}$.

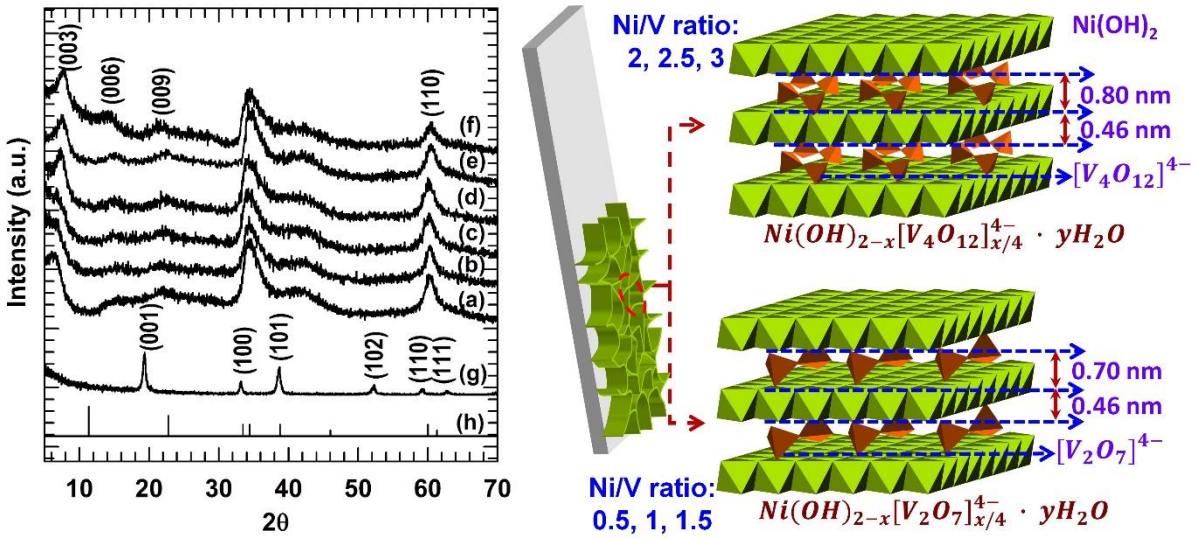

Fig. 1 (Left) XRD patterns of (a) LNHV-3, (b) LNHV-2.5, (c) LNHV-2, (d) LNHV-1.5, (e) LNHV-1, (f) LNHV-0.5, (g) LNHV-0, and (h) $Ni(OH)_2$ (JCPDS 38-0715). (Right) Structural schematic model of the LNHV nanohybrids.

To probe the effect of the pillared polyoxovanadate content on the physicochemical properties, $Ni(OH)_2$−POV nanohybrids are synthesized with various nickel/vanadium precursor ratios of 0, 0.5, 1, 1.5, 2, 2.5, and 3, and the obtained $Ni(OH)_2$−POV nanohybrids are denoted as LNHV-0, LNHV-0.5, LNHV-1, LNHV-1.5, LNHV-2, LNHV-2. 5, and LNHV-3, respectively. The evolution of the crystallographic structure of the pristine $Ni(OH)_2$, namely LNHV-0, upon the pillaring of the 0D polyoxovanadate is studied using the powder XRD analysis. Figure 1 represents the powder XRD patterns of the $Ni(OH)_2$−POV nanohybrids. The LNHV-0 sample displays a series of well-developed {00l} Bragg reflections of the turbostratic β-$Ni(OH)_2$ structure. The lattice parameters of the β-$Ni(OH)_2$ of a = 0.31 nm and c = 0.46 nm are determined according to the least-squares fitting analysis, which is in good agreement with the lattice parameters of the β-$Ni(OH)_2$ structure.[20,37] Similar to the β-$Ni(OH)_2$, all of the $Ni(OH)_2$−POV materials display a series

of well-developed {00l} Bragg reflections at the low 2θ regions, indicating the formation of a layer-by-layer ordered pillared structure with an expanded basal spacing. According to the least-squares fitting analysis, the basal spacing of the $Ni(OH)_2$−POV is estimated to be from 1.31 nm to 1.16 nm. The expanded basal spacing of the $Ni(OH)_2$−POV demonstrates the intercalation of the polyoxovanadium species that are between the host $Ni(OH)_2$ sheets. The basal spacing decreases gradually from 1.31 to 1.16 as the Ni/V ratio decreases from 3 to 1.5. For the Ni/V ratios below 1.5, a constant value of 1.16 is obtained. The larger basal spacing for higher reactant ratios clearly indicates the intercalation of the more condensed polyoxovanadium species $[V_4O_{12}]^{4-}$, which is due to a rapid fall in the pH to ~ 8 during a given deposition time (a rapid drop in the pH from 13 to 8 corresponds to a Ni/V reactant ratio from 3 to 2). However, for the other reactant Ni/V ratios below 2, a pH reduction occurs slowly from 13 to ~ 10, which leads to the decrease of the basal spacing of 1.16, and this is ascribed to the less condensed polyoxovanadium species $[V_2O_7]^{4-}$. The thickness of the $Ni(OH)_2$−POV crystallite along the *c*-axis is estimated to be ~ 5 nm to ~ 6 nm using the Scherrer calculation with the full-width-at-half-maximum (FWHM) of {001} reflections. This finding suggests that these crystallites are nanosheets consisting of ~ 3 to ~ 4 POV-pillared $Ni(OH)_2$ monolayers. For the hexagonal $Ni(OH)_2$ sheets, all of the $Ni(OH)_2$−POV show an in-plane (110) peak and a broad hump peak at 2θ = ~ 60.4° and 2θ = ~ 32° to 44°, respectively, which highlights the maintenance of the in-plane structure of the $Ni(OH)_2$ with a turbostratic structure.

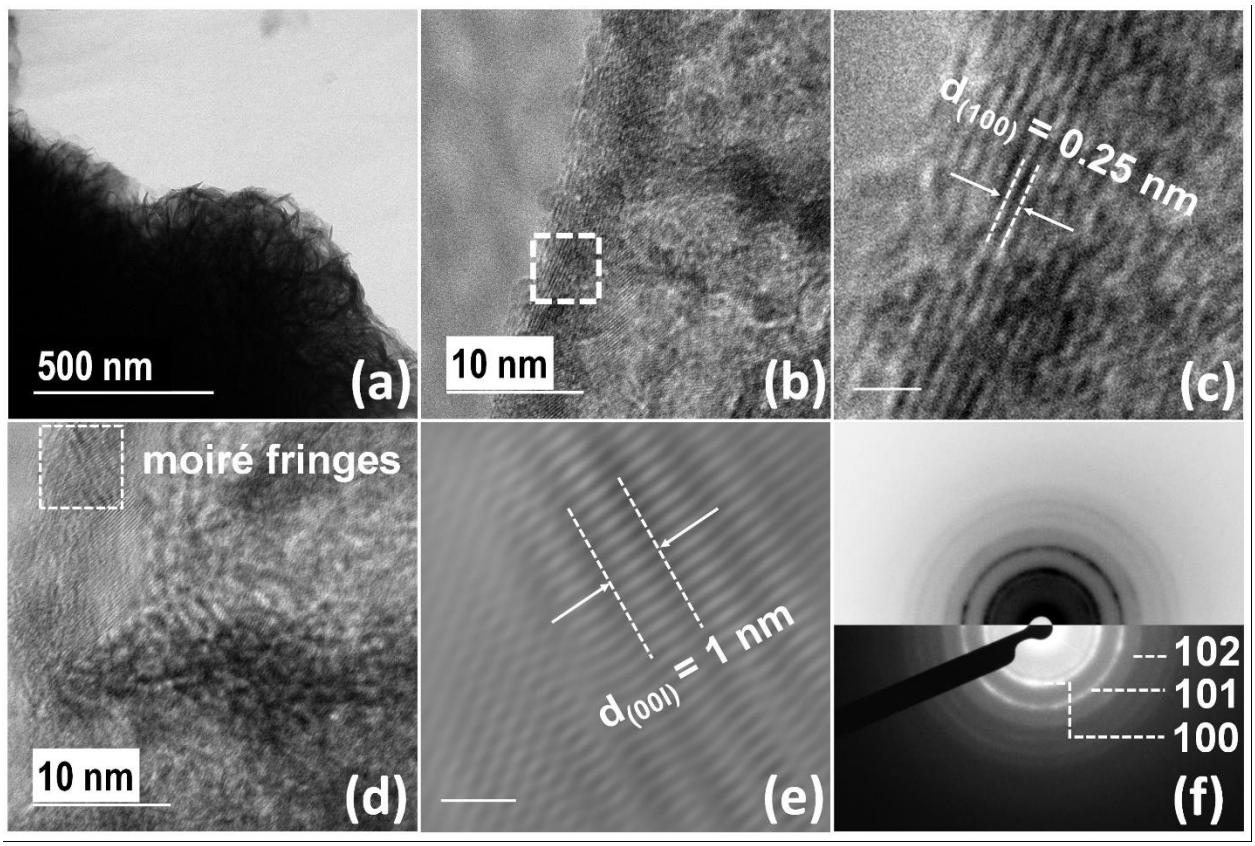

Fig. 2 (a,b) TEM and (c) HRTEM images of the $Ni(OH)_2$−POV (LNHV-1 sample); (d,e) TEM and HRTEM images exemplifying the moiré fringe patterns from the as-prepared $Ni(OH)_2$−POV. (f) SAED pattern of the $Ni(OH)_2$−POV; The scale bars in the HRTEM images are equal to 1 nm.

The local crystal structure, morphology, and formation of the layer-by-layer-ordered nature of the as-prepared $Ni(OH)_2$-POV are determined by the HRTEM and the selected area electron diffraction (SAED) analyses. As illustrated in Figs. 2 (a) and (b), the low-magnification TEM images of the $Ni(OH)_2$-POV **(LNHV-1)** demonstrate the interconnected house-of-cards-type network of the hetero-layered $Ni(OH)_2$-POV crystallites. The series of equally-spaced fringes that correspond to the host $Ni(OH)_2$ hexagonal lattice are observed, as shown in Fig. 2(c). The interline

distance between the two consecutive lattice fringes is approximately 0.25 nm, and this value is in good agreement with the hexagonal $Ni(OH)_2$ bulk value (JCPDS 38-0715).[37] The development of a well-ordered moiré-fringe pattern depicts the formation of the layer-by-layer-ordered structure of $Ni(OH)_2$ nanosheets that are intercalated with isopolyoxovanadate. These lattice distances between these fringes are separated by a distance of ~ 1 nm, which is attributed to the expanded $Ni(OH)_2$ gallery after the intercalation of the 0D isopolyoxovanadate nanoclusters. The estimated moiré-fringe spacing is in good agreement with the *c*-axis lattice parameter determined from the XRD analysis.[38] The present assignment is further confirmed by the HRTEM and SAED analyses. As shown in Fig. 2(f), a typical hexagonal pattern diffraction feature is resolved from the as-prepared crystals.[39] As highlighted in Figure 2(f), the sharp diffraction rings can be assigned as the (100), (101), and (102) reflection from the host-$Ni(OH)_2$ crystals. Besides the sharp diffraction rings, several diffuse and broad rings are also observed. These rings are identified as the diffraction arising from the polycrystalline polyoxovanadate nanoclusters which are stabilized within the $Ni(OH)_2$ nanosheets.[39]

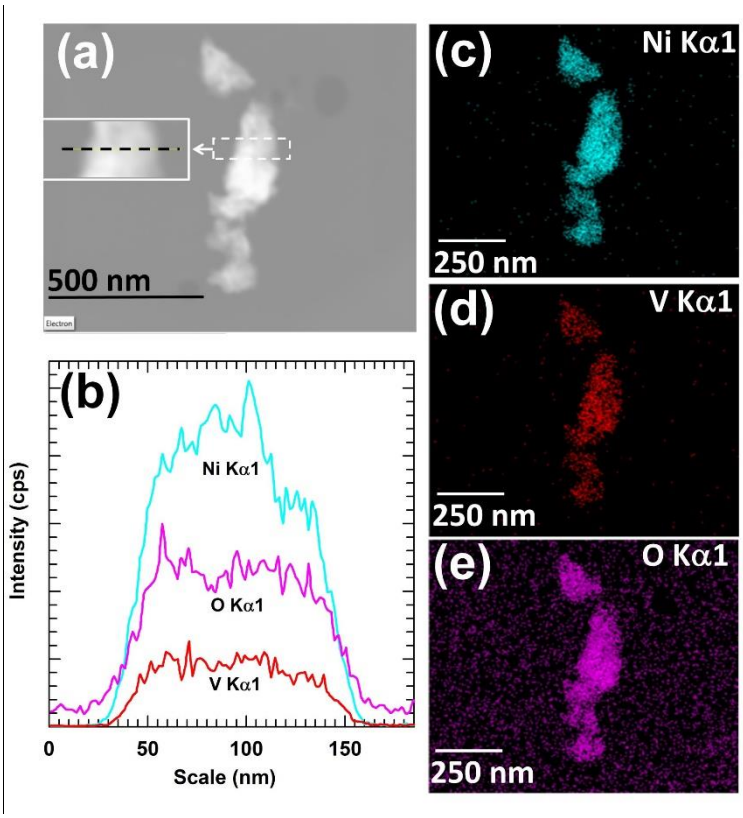

Fig. 3. (a) HAADF STEM image of as-prepared $Ni(OH)_2$-POV, (b) element line scans along the dotted line in (a) and HAADF STEM element mapping for (c) Ni, (d) V, and (e) O in the $Ni(OH)_2$-POV (LNHV-1) nanohybrid.

Moreover, the localized elemental distributions in the $Ni(OH)_2$–POV nanosheets are investigated using high angle annular dark field (HAADF) scanning transmission electron microscope (STEM). In Figs. 3(a, b), the elemental EDS line-scan profile which is generated from a randomly selected region exhibits the vertically homogeneous distributions of nickel (Ni), vanadium (V) and oxygen (O) elements. The HAADF-STEM element-mapping results in Figs. 3 (c) to (e) further confirm the intimate and lateral homogeneous intercalation of POV nanoclusters into the interlayer of the $Ni(OH)_2$ nanosheets.

FE-SEM and EDS/Elemental Mapping Analyses

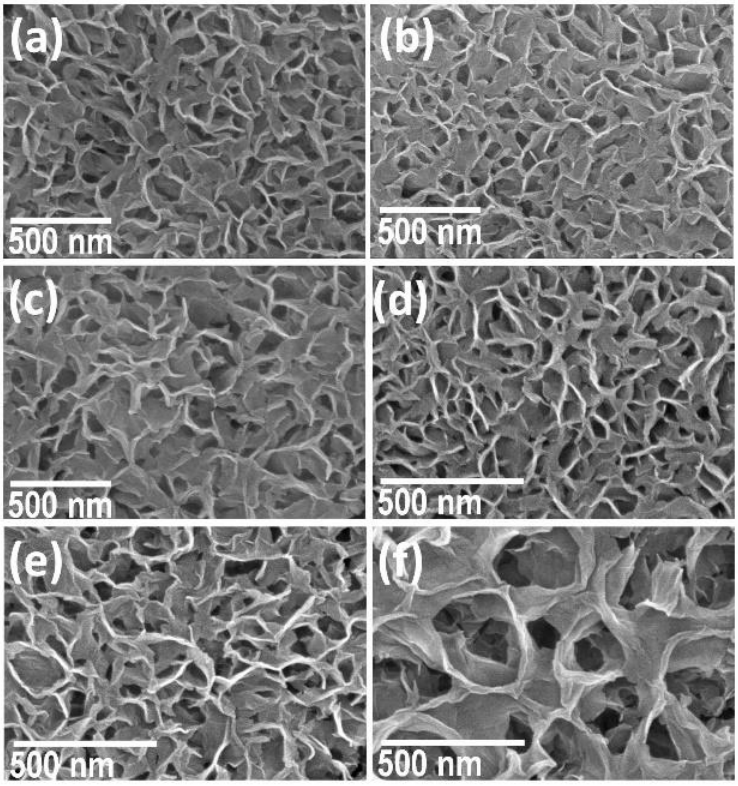

Fig. 4. FE-SEM images of the $Ni(OH)_2$−POV thin films deposited on stainless steel with different POV loadings: (a) LNHV-3, (b) LNHV-2.5, (c) LNHV-2, (d) LNHV-1.5, (e) LNHV-1, and (f) LNHV-0.5.

The crystal morphology and size of the $Ni(OH)_2$−POV thin films fabricated on the stainless steel substrates are characterized by field-emission scanning electron microscopy (FE-SEM). As presented in Fig. 4, all of the $Ni(OH)_2$−POV thin films display nanosheets that are vertically grown on the substrate surface. The interconnected nanosheets form a mesoporous house-of-cards-type morphology. A careful inspection reveals that the thicknesses of the $Ni(OH)_2$−POV nanosheets are from 5 nm to 15 nm, and the edges are slightly scrolled to minimize the surface energy. Such

a nanosheet morphology is commonly observed for CSD-deposited hydroxide materials.[40,41] The estimated thicknesses of 5 nm to 15 nm suggest the presence of approximately 3 to 6 stacked layers of 2D $Ni(OH)_2$ with the polyoxovanadate. The intercalation of the polyoxovanadate is further confirmed using the EDS and elemental analyses (Supplementary Information). All of the constituent elements, i.e., nickel (Ni), vanadium (V) and oxygen (O), are uniformly distributed across all the $Ni(OH)_2$−POV thin films, which re-confirms that the intercalation of the polyoxovanadate nanoclusters in the gallery spacing of the $Ni(OH)_2$ nanosheets are homogeneous and without any spatial-phase separation. The EDS elemental analysis demonstrates the tuning of the chemical composition of the $Ni(OH)_2$−POV thin films (Supplementary Information).

FT-IR and Micro-Raman Spectroscopy

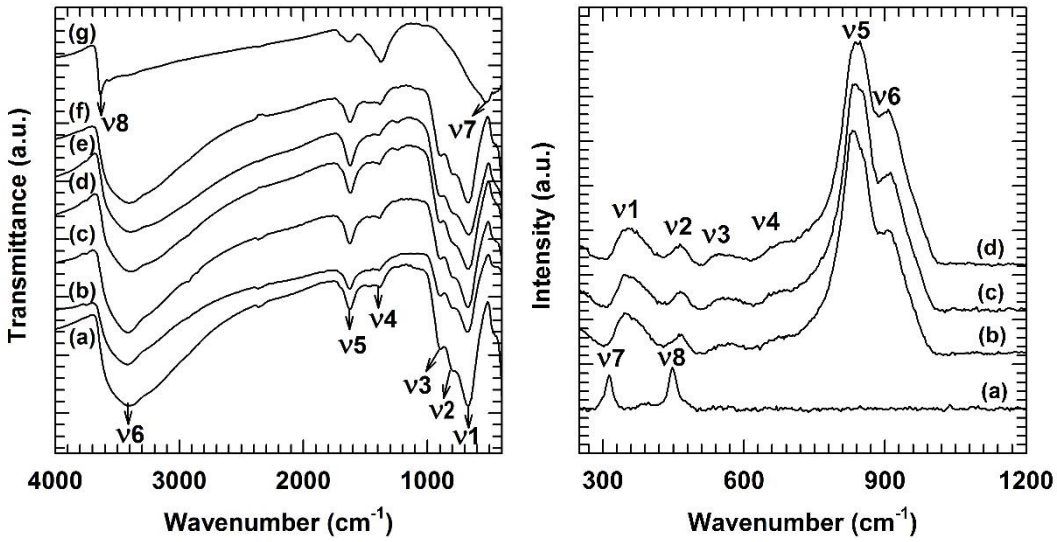

Fig. 5. (Left) FT-IR spectra of the $Ni(OH)_2$−POV thin films: (a) LNHV-3, (b) LNHV-2.5, (c) LNHV-2, (d) LNHV-1.5, (e) LNHV-1, (f) LNHV-0.5, and (g) LNHV-0. (Right) Micro-Raman spectra of the $Ni(OH)_2$−POV thin films: (a) LNHV-3, (b) LNHV-1.5, (c) LNHV-0.5, and (d) LNHV-0.

The chemical bonding nature of the polyoxovanadium species in the $Ni(OH)_2$−POV thin films is examined with Fourier transform infrared (FT-IR) spectroscopy. As plotted in Fig. 5 (left), all of the $Ni(OH)_2$−POV thin films show very similar spectral features. The strong and sharp absorption peak at ν1 (670 cm^{-1}) and the shoulder band at ν2 (810 cm^{-1}) are attributed to the antisymmetric and symmetric stretching modes of the V-O-V chains, respectively.[42] Furthermore, the second shoulder band at a higher wavenumber ν3 (910 cm^{-1}) is assigned to the symmetric stretching mode of the terminal V=O groups.[43,44] The presence of these bands confirms the incorporation of the polyoxovanadate ions into the interlayer space of the $Ni(OH)_2$.[45-47] It should be noted that a mild band ν4 (1386 cm^{-1}) is presented among all samples, which is attributed to the absorbed carbonate moieties on the external surface of the particles due to the high pH of the CSD. The other IR bands at ν6 (3420 cm^{-1}) and ν5 (1600 cm^{-1} to 1630 cm^{-1}) are assigned to the $Ni(OH)_2$ and the free H_2O O-H stretching and bending modes respectively.[48]

Micro-Raman spectroscopy is also employed to further probe the successful intercalation of polyoxovanadate. As indexed in Fig. 5 (right panel), the as-prepared nano hybrid thin films exhibit ν1 to ν10 characteristic Raman peaks that belong to the characteristic Raman shift from the 0D-POV species (see Supplementary Information for details). These characteristic features underscore the intercalation of the 0D-POV species inside the $Ni(OH)_2$ gallery. The peaks at 330 cm^{-1} and 460 cm^{-1} are attributed to the E_g and A_{1g} lattice modes of the $Ni(OH)_2$. The LNHV-0 nanohybrid with no POV revealed peaks at 313 and 448 cm-1 without any POV signature peak, and they are attributed to the Raman-active vibrations of the E_g and A_{1g} modes of the β-$Ni(OH)_2$, respectively. The peak at 540 cm^{-1} is attributed to the second-order acoustic mode of $Ni(OH)_2$. A weak peak feature centred at 1617 cm^{-1} is composed of the superposition of the O-H bending mode of the

intercalated water at 1600 cm^{-1} and the surface-adsorbed/structure-trapped water at 1630 cm^{-1}. The broad signature peak from 3500 cm^{-1} to 3690 cm^{-1} is attributed to the internal O−H stretching modes from the lattice OH and the intersheet H_2O. All of the LNHV nanohybrids show a high-intensity broad peak centred at 838 cm^{-1} with the signature shoulder at 910 cm^{-1}. The observed feature is the superposition of three characteristic peaks at 790 cm^{-1}, 838 cm^{-1}, and 910 cm^{-1}, which are attributed to the second-order lattice mode of the α-$Ni(OH)_2$, and the symmetric-stretching vibrational modes of the $[V_2O_7]^{4-}$ and $[V_4O_{12}]^{4-}$, respectively. A careful observation of the peaks highlights a trend of a signal shifting to lower frequencies, and this is attributed to the decreasing polyoxovanadium chain length. The observed Raman features indicate the intercalation of the $[V_2O_7]^{4-}$ in the nanohybrids of the LNHV-0.5 to LNHV-1.5 and the $[V_4O_{12}]^{4-}$ in the nanohybrids of the LNHV-2 to LNHV-3.

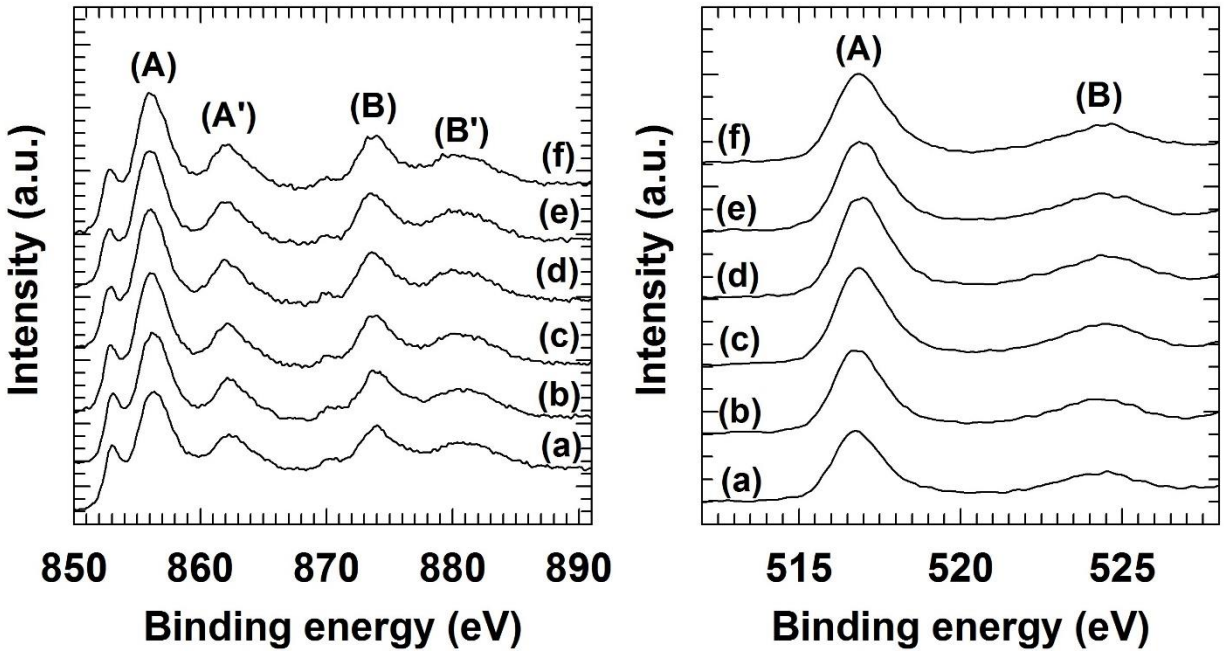

Fig. 6. (Left) Ni 2p and (right) V 2p core-level XPS spectra of the $Ni(OH)_2$−POV thin films: (a) LNHV-3, (b) LNHV-2.5, (c) LNHV-2, (d) LNHV-1.5, (e) LNHV-1, and (f) LNHV-0.5.

Various chemical oxidation states of the intercalated polyoxovandium species and their effect on the chemical bonding nature of the host $Ni(OH)_2$ lattice are uncovered by performing XPS measurements. As illustrated in Fig. 6 (left), all of the $Ni(OH)_2$−POV thin films show two spectral features that arise from the spin–orbit splitting of the Ni p orbital, both of which are assigned to Ni $2p_{3/2}$ and Ni $2p_{1/2}$, respectively, as follows: A at 856.15 eV and B at 873.7 eV. The A and B peaks are separated by a spin-energy difference of 17.6 eV with significant satellite peaks A′ and B′ at 862 eV and 880 eV, respectively, both of which are characteristic signatures of the Ni^{2+} in the $Ni(OH)_2$ phase.[49-52] The V 2p XPS spectra of the $Ni(OH)_2$−POV thin films are illustrated in Fig. 6 (right). All of the LNHV thin films show two spectral features that arise from the spin–orbit splitting at A (513 eV to 519 eV region) and B (521 eV to 526 eV region) and correspond to V $2p_{3/2}$ and V $2p_{1/2}$, respectively, thereby yielding a binding energy difference of **7.2 eV**. A careful inspection of the V 2p3/2 peak suggests that the construction of the broad peak A consists of two peaks. The high intensity at **817** eV is attributed to the pentavalent vanadium in the intercalated polyoxovanadium.[53,54]

Electrochemical Measurements

The effects of the intercalation of the isopolyoxomatalates on the capacitance behaviors of the host $Ni(OH)_2$ nanosheets are examined using the cyclic voltammetry (CV), galvanostatic charge discharge (GCD), and impedance analyses. The electrochemical characteristics of the $Ni(OH)_2$−POV supercapacitors are investigated using a three-electrode electrochemical cell in

which the $Ni(OH)_2$−POV thin films are used as the working electrode, a platinum mesh serves as the counter and a saturated calomel electrode (SCE) serves as the reference electrode. **Figure 7** represents the CV curves of the $Ni(OH)_2$−POV thin film electrodes.

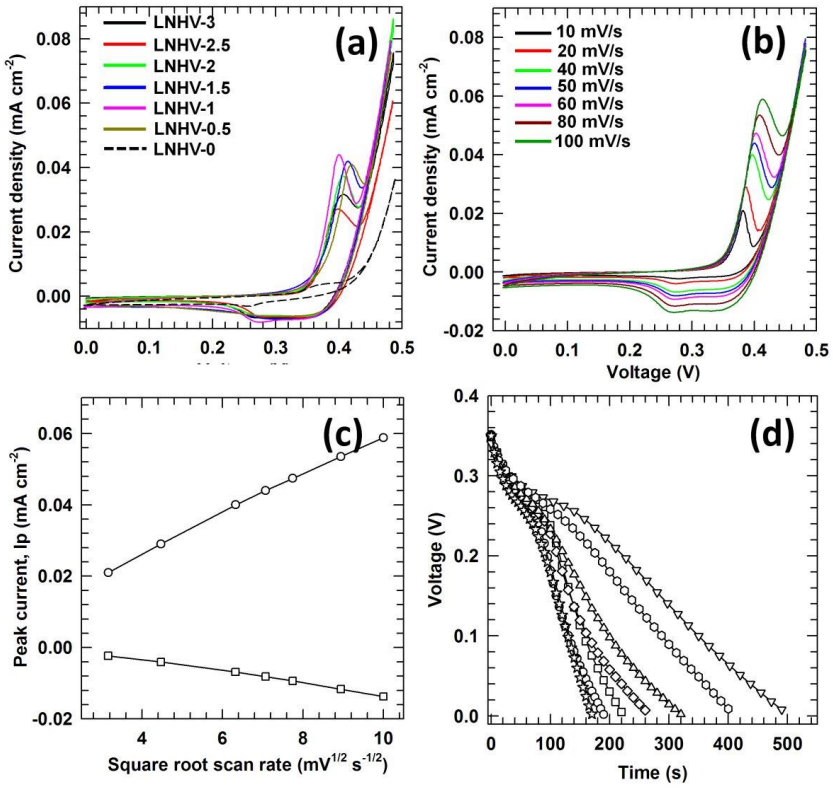

Fig. 7. (a) CV curves of the $Ni(OH)_2$−POV thin film electrodes at a scan rate of 50 mV/s. (b) CV curves of the $Ni(OH)_2$−POV (LHNV-1) thin film electrodes at various scan rates. **(c)** Oxidation and reduction peak currents as a function of the square root of the scan rate for the $Ni(OH)_2$−POV (LHNV-1) thin film electrode. **(d)** GCD curves of the $Ni(OH)_2$−POV thin film electrodes of the LNHV-3 (circle), LNHV-2.5 (square), LNHV-2 (diamond), LNHV-1.5 (triangle-up), LNHV-1 (triangle-down), LNHV-0.5 (hex), and LNHV-0 (star) at 1 mA/g.

All of the intercalated $Ni(OH)_2$−POV thin film electrodes display typical discernible redox peaks that correspond to the Faradaic redox reactions between $Ni(OH)_2$ and NiOOH. This demonstrates that the electrochemical activity of these electrodes mainly originates from the pseudocapacitive behavior that is based on the following redox mechanism:

$$Ni(OH)_2 + OH^- \rightarrow NiOOH + H_2O + e^- \quad (???)$$

The POV intercalation remarkably increases the integral area of the CV curves of the pristine $Ni(OH)_2$ thin film electrode, as shown in Fig. 7(a), which highlights the crucial role of the POV intercalation in the improvement of the electrochemical activity of the $Ni(OH)_2$−POV. Among the $Ni(OH)_2$−POV thin film electrodes, LNHV-1 has the largest area, which highlights its superior electrochemical performance.

Figure 7(b) shows the CV curves at different scan rates ranging from 10 mV/s to 100 mV/s for the LNHV-1 electrode. As the scan rate increases, the cathodic peak current also increases, indicating its pseudocapacitive behavior. As shown in Fig. 7(c), the linear increase of the redox peak current densities demonstrates a pseudocapacitive behavior that is limited by the diffusion controlled electrochemical reaction of the $Ni(OH)_2$−POV electrode.

The electrochemical performance of the $Ni(OH)_2$−POV thin film electrode (LNHV-1) is further evaluated by measuring its galvanometric charge-discharge properties. As illustrated in Fig. 7(d), all of the $Ni(OH)_2$−POV thin film electrodes show typical nonlinear charge-discharge behaviours. This implies that the reversible Faradaic reactions significantly contribute to the specific capacitance of the $Ni(OH)_2$−POV thin film electrodes. The specific capacitance value obtained from the LNHV-3, LNHV-2.5, LNHV-2, LNHV-1.5, LNHV-1, LNHV-0.5, and LNHV-0 $Ni(OH)_2$−POV samples is 536 F/g, 637 F/g, 771 F/g, 897 F/g, 1440 F/g, 1170 F/g, and 611 F/g respectively. All of the intercalated $Ni(OH)_2$−POV thin film electrodes demonstrate considerably

enhanced specific capacitance compared with the pristine $Ni(OH)_2$, which highlights the advantage of the POV intercalation for the improvement of the electrochemical supercapacitor activity. The observed improvement of the supercapacitor performance upon the intercalation with the POV nanoclusters is attributable to the expanded interlayer gallery height of the host $Ni(OH)_2$ nanosheet lattice, which leads to an increase in the freely accessible interlayer gallery space for the redox-reaction electrolyte ions. The mesoporous house-of-cards morphology of the $Ni(OH)_2$−POV thin film electrodes additionally contributes to the redox reactions by enhancing the efficient adsorption of the electrolyte ions. The specific capacitance is increased from 536 F/g for the sample with a higher POV content (LNHV-3), it reaches the maximum value of 1440 F/g for the sample with an optimum POV content (LNHV-1) and again it decreases to 1170 F/g for the sample with the lowest POV content (LNHV-0.5). This finding elucidates the crucial role of the intercalated POV species in determining the supercapacitor performance of the $Ni(OH)_2$−POV thin film electrodes. The experimental results provide strong evidence for the tunability of the supercapacitor performance of the $Ni(OH)_2$-based nanohybrid electrodes through the selection of the intercalated POV content.

To probe the effective charge-discharge mechanism of the $Ni(OH)_2$−POV thin film electrodes, the dependence of the specific capacitance of the $Ni(OH)_2$−POV thin film electrodes on the current density is examined (see ESI). As illustrated in Fig. **S3**, all of the electrodes show a decrease in the specific capacitance with an increasing charge–discharge current density. The capacitive behaviour of the layered inorganic materials is governed by the following two contributing mechanisms: the adsorption/desorption of the solvated ions on the surface of the layered inorganic material and the intercalation/de-intercalation of the solvated ions into/out of the interlayer space of the layered electrode material. The observed decrease in the specific capacitance with the current density is ascribed to the diffusion effect of the solvated electrolyte

ions within the expanded gallery of the $Ni(OH)_2$–POV electrode, where inner active sites cannot precede the redox transition completely at high current densities. The intercalation of the POV nanoclusters provides an expanded interlayer gallery space that leads to a considerably enhanced diffusion of the solvated electrolyte ions. Conversely, intercalation of the POV nanoclusters beyond a critical value implies a decrease in the free gallery space for the solvated electrolyte ions to move freely, which is detrimental to the capacitive performance of the $Ni(OH)_2$–POV electrode. A rapid fading of the specific capacitance with an increasing charge-discharge current density in the samples with a low POV content (LNHV-0.5 and LNHV-1) suggests that the diffusion controlled pseudocapacitive charge storage mechanism plays a dominant role in these samples. Therefore, the largest specific capacitance of the LNHV-1 electrode with an intermediate initial Ni/V precursor ratio is due to the best optimised POV content among the present $Ni(OH)_2$–POV thin film electrodes. The LNHV-1 electrode demonstrates a superior electrochemical stability over 2000 cycles with an excellent capacity retention of 85% (see ESI).

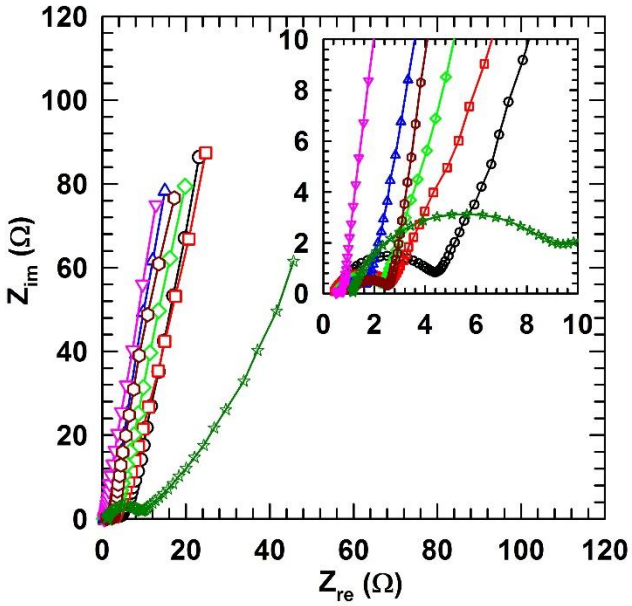

Fig. 8. Nyquist plots of the $Ni(OH)_2$−POV thin film electrodes. (circle) LNHV-3, (square) LNHV-2.5, (diamond) LNHV-2, (triangle-up) LNHV-1.5, (triangle-down) LNHV-1, (hex) LNHV-0.5, and (star) LNHV-0. The inset shows an enlarged view of the EIS spectra in the high frequency region.

To further elucidate the charge transport mechanisms that contribute to the superior electrochemical activity of the $Ni(OH)_2$−POV thin film electrodes, EIS measurements are conducted. Figure 8 shows the Nyquist plots for the $Ni(OH)_2$−POV thin film electrodes. All of the electrodes show partially overlapping semicircles in the high-frequency region. The presence of a semicircle is linked to the resistance of the electrolyte (R_e) and the charge transfer resistance (R_{ct}). All of the $Ni(OH)_2$−POV thin film electrodes show much smaller R_e values compared with the pristine $Ni(OH)_2$ electrode, which indicates the improvements in the charge transfer and the electrical conductivity with the POV intercalation. The $Ni(OH)_2$−POV electrode with the optimised POV content (LNHV-1) has the smallest semi-circle compared with the other electrodes. As discussed earlier, because the surface areas of all of the electrode materials are comparable, the size of the arches is likely to be determined by the electrical conductivity of the $Ni(OH)_2$−POV electrodes. The inclined lines in the low-frequency region correspond to the Warburg impedance, which is associated with the diffusion of the electrolyte ions into the bulk electrodes. Compared with the bare $Ni(OH)_2$ electrode (LNHV-0), the slopes of the other $Ni(OH)_2$−POV samples are much larger, and this implies a lower resistance for the diffusion of the electrolyte ions throughout the electrode. Therefore, the performance enhancement in the $Ni(OH)_2$−POV electrode is due to the improved electrical conductivity and diffusion of the electrolyte ions.

Conclusion

In summary, an interconnected network of 2D $Ni(OH)_2$ nanosheets that are intercalated with 0D polyoxovandate nanoclusters was fabricated using chemical solution deposition, and it exhibited a promising applicability as a binder-free electrode for the improvement of the electrochemical activity of bare $Ni(OH)_2$. Given that the pristine $Ni(OH)_2$ phase is one of the most efficient supercapacitor electrodes, the presented $Ni(OH)_2$−POV nanohybrids showed a significantly enhanced level of electrochemical-activity as a supercapacitor electrode, thereby underscoring the beneficial effect of the POV intercalation on the supercapacitor performance of the pristine metal hydroxide material. The highest specific capacitance of 1400 Fg^{-1} was obtained from the most optimized $Ni(OH)_2$−POV electrode. We attributed the remarkable enhancement of the electrochemical energy storage ability of the pristine $Ni(OH)_2$ with the POV intercalation not only to the formation of a highly porous house-of-cards-type interconnected network morphology but also to an increased freely accessible gallery space and electrical conductivity. This study demonstrated the effectiveness of the chemical solution deposition (CSD) method for the deposition of highly porous metal hydroxide materials that are intercalated with 0D polyoxomatalate for exploring efficient hydroxide-based electrode materials. Taking into account the fact that it is possible that CSD-deposited $Ni(OH)_2$ materials might boast numerous excellent functionalities, like electrochemical water splitting and battery electrodes, the intercalation of the 0D polyoxomatalates into the host matrix can provide a universal methodology for the CSD-based deposition of novel functional materials from the reported OH_2 deposition database. This synthetic CSD-based strategy is readily extendible for diverse couples of metal hydroxide nanosheets and anionic 0D nanoclusters. Currently, the exploration of efficient electrochemical energy harvesting

from the intercalated assembly between $Ni(OH)_2$ and other 0D polyoxomatalate nanoclusters is underway.

Experimental Section

Materials. Nickel chloride ($NiCl_2$), Sodium orthovanadate (Na_3VO_4), and ammonium hydroxide (NH_4OH; 28 %), were purchased from Sigma-Aldrich and used without further purification. Stainless steel (SS) substrates were used for the deposition of the $Ni(OH)_2$−POV thin films.

Experimental Details.

The chemical bath for the deposition of the $Ni(OH)_2$−POV comprised an aqueous solution of 0.1 M $NiCl_2$ that was combined with an aqueous NH_3 solution (6.5 M; 2.5 mL) under constant stirring. During addition of NH_3, an initially apple-green coloured precipitate, the $Ni(OH)_2$ was formed, which was subsequently dissolved back into the solution by the further addition of an excess NH_3 solution. The pH of the solution at this stage was ~12.5. For a vanadium (V) precursor, an aqueous solution of 0.1M Na_3VO_4 was prepared. The chemical deposition bath was obtained by the mixing of the stock solutions into a 50 mL glass beaker with the sequential addition of 20 ml of a Ni-amine complex and the requisite amount of the V precursor. The final pH of the bath was adjusted to ~ 13 using the aqueous NH_3. Since the substrate provided nucleation centres for the

heterogeneous growth of the deposited material, the cleaning step of the substrate played a crucial role in the successful deposition of the uniform film. The stainless steel substrates were cleaned with zero grade polish paper followed by washing with de-ionized water. After the cleaning process, the substrates were stored in distilled water to avoid any possible dust contamination. Before the film deposition, the substrates were again cleaned with distilled water and dried with an Ar flow. A pre-cleaned SS substrate was immersed and placed vertically in the solution. The solution was maintained at a pH of approximately 13 and a temperature of 50 °C for 3 h, resulting in the direct growth of the LNHV nanosheet network on the glass substrate. After the deposition, the LNHV nanosheet-deposited substrates were retrieved from the bath, washed with the deionized water, and dried under the Ar flow. The bulk LNHV samples formed using homogeneous precipitation were collected from the same bath using successive centrifugation and washing procedures.

The crystal structures of the LNHV thin film were examined using the powder X-ray diffraction (XRD) analysis for which a Rigaku diffractometer with Ni-filtered Cu Kα (Kα = 1.54056 A) radiation was employed. The surface morphology, nanosheet size, and elemental distribution of the LNHVs were probed with the use of FE-SEM (Hitachi S-4800) for which is equipped with energy-dispersive spectrometry (EDS). For further insight into the microstructure of the LNHV nanosheets, transmission electron microscopy (TEM), high-resolution TEM (HRTEM) and selected area electron diffraction (SAED) images are recorded using the JEOL-3000F at 300 kV with a camera length of 255.8 mm. High angle annular dark field (HAADF) scanning transmission electron microscope (STEM) and element mapping were carried out at 200 kV using a JEOL-2010 microscope with an X-ray EDS accessory. The Fourier-transform infra-red (FT-IR) spectroscopic analysis was performed in a frequency range of 400 cm^{-1} to 4000 cm^{-1}

using the Jasco FT/IR-6100 FT spectrometer, and this allowed us to study the chemical bonding nature of the LNHV nanosheets. The Raman spectra were recorded with the Horiba Jobin-Yvon LabRam Aramis spectrometer. The 514 nm line of an Ar-ion laser was used as the excitation source.

Electrochemical measurements

The electrochemical activity of the LNHV nanosheet thin films was investigated using cyclic voltammetry (CV), galvanostatic charge/discharge (GCD), and electrochemical impedance spectroscopy (EIS) analysis. All of the electrochemical measurements were carried out using the electrochemical workstation Versa-stat-3 (Princeton Applied Research) with a standard three electrode electrochemical cell. Precisely deposited unit area LNHV nanosheet thin films, a saturated calomel electrode (SCE), and a platinum mesh served as the working, reference, and counter electrodes, respectively. An aqueous solution (2 M) of potassium hydroxide (KOH) was employed as the electrolyte.

Acknowledgements

This research is supported by the National Research Foundation (NRF) of Korea (Grant nos. 2016R1A6A1A03012877, 2015M2A2A6A02045251, 2015R1A2A2A01004782, 2015R1D1A1A01058851 and 2015R1D1A1A01060743).

Electronic Supplementary Information (ESI) available:

Characterization results including EDS, EDS-elemental mapping, micro-Raman, electrochemical performance high current density, electrochemical stability.

1. K. L. Choy, *Progress in Materials Science*, 2003, **48**, 57-170.
2. R. S. Mane and C. D. Lokhande, *Materials Chemistry and Physics*, 2000, **65**, 1-31.
3. C. Liu, F. Li, L. P. Ma and H. M. Cheng, *Advanced Materials*, 2010, **22**, E28-+.
4. Y. Xiang, S. F. Lu and S. P. Jiang, *Chem Soc Rev*, 2012, **41**, 7291-7321.
5. J. R. Miller and P. Simon, *Science*, 2008, **321**, 651-652.
6. D. P. Dubal, O. Ayyad, V. Ruiz and P. Gomez-Romero, *Chem Soc Rev*, 2015, **44**, 1777-1790.
7. G. Wang, L. Zhang and J. Zhang, *Chem Soc Rev*, 2012, **41**, 797-828.
8. U. Patil, S. C. Lee, S. Kulkarni, J. S. Sohn, M. S. Nam, S. Han and S. C. Jun, *Nanoscale*, 2015, **7**, 6999-7021.
9. A. I. Inamdar, Y. Kim, S. M. Pawar, J. H. Kim, H. Im and H. Kim, *J Power Sources*, 2011, **196**, 2393-2397.
10. T. H. Gu, J. L. Gunjakar, I. Y. Kim, S. B. Patil, J. M. Lee, X. Jin, N. S. Lee and S. J. Hwang, *Small*, 2015, **11**, 3921-3931.
11. A. I. Inamdar, Y. S. Kim, J. S. Sohn, H. Im, H. Kim, D. Y. Kim, R. S. Kalubarme and C. Park, *J Korean Phys Soc*, 2011, **59**, 145-149.
12. J. L. Gunjakar, I. Y. Kim, J. M. Lee, Y. K. Jo and S. J. Hwang, *Journal of Physical Chemistry C*, 2014, **118**, 3847-3863.
13. D. H. Park, S. J. Hwang, J. M. Oh, J. H. Yang and J. H. Choy, *Prog Polym Sci*, 2013, **38**, 1442-1486.
14. K. Yan, G. S. Wu and W. Jin, *Energy Technol-Ger*, 2016, **4**, 354-368.
15. Q. Wang and D. O'Hare, *Chem Rev*, 2012, **112**, 4124-4155.
16. G. L. Fan, F. Li, D. G. Evans and X. Duan, *Chem Soc Rev*, 2014, **43**, 7040-7066.
17. X. Long, Z. L. Wang, S. Xiao, Y. M. An and S. H. Yang, *Mater Today*, 2016, **19**, 213-226.
18. U. M. Patil, J. S. Sohn, S. B. Kulkarni, S. C. Lee, H. G. Park, K. V. Gurav, J. H. Kim and S. C. Jun, *Acs Applied Materials & Interfaces*, 2014, **6**, 2450-2458.
19. V. Rives, *Layered double hydroxides : present and future*, Nova Science Publishers, Huntington, N.Y., 2001.
20. P. V. Kamath, G. H. A. Therese and J. Gopalakrishnan, *J Solid State Chem*, 1997, **128**, 38-41.
21. Y. Du and D. O'Hare, *Inorg Chem*, 2008, **47**, 3234-3242.
22. J. Demel, J. Hynek, P. Kovar, Y. Dai, C. Taviot-Gueho, O. Demel, M. Pospisil and K. Lang, *Journal of Physical Chemistry C*, 2014, **118**, 27131-27141.
23. E. Gardner, K. M. Huntoon and T. J. Pinnavaia, *Advanced Materials*, 2001, **13**, 1263-1266.
24. X. X. Guo, F. Z. Zhang, D. G. Evans and X. Duan, *Chemical Communications*, 2010, **46**, 5197-5210.
25. R. Z. Ma, Z. P. Liu, L. Li, N. Iyi and T. Sasaki, *Journal of Materials Chemistry*, 2006, **16**, 3809-3813.
26. L. Mohapatra, K. Parida and M. Satpathy, *Journal of Physical Chemistry C*, 2012, **116**, 13063-13070.
27. S. K. Yun and T. J. Pinnavaia, *Inorg Chem*, 1996, **35**, 6853-6860.
28. S. Omwoma, W. Chen, R. Tsunashima and Y. F. Song, *Coordin Chem Rev*, 2014, **258**, 58-71.
29. D. G. Evans and D. A. Xue, *Chemical Communications*, 2006, DOI: 10.1039/b510313b, 485-496.
30. L. Li, R. Z. Ma, Y. Ebina, K. Fukuda, K. Takada and T. Sasaki, *J Am Chem Soc*, 2007, **129**, 8000-8007.
31. G. Hodes, *Chemical solution deposition of semiconductor films*, Marcel Dekker, New York, 2003.

32. C. F. Baes and R. E. Mesmer, *The hydrolysis of cations*, R.E. Krieger, Malabar, Fla., 1986.
33. Y. G. Li, B. Tan and Y. Y. Wu, *Chemistry of Materials*, 2008, **20**, 2602-2602.
34. I. Ichinose, K. Kurashima and T. Kunitake, *J Am Chem Soc*, 2004, **126**, 7162-7163.
35. C. F. Baes and R. E. Mesmer, *The hydrolysis of cations*, Wiley, New York, 1976.
36. J. Livage, *Coordin Chem Rev*, 1998, **178**, 999-1018.
37. D. S. Hall, D. J. Lockwood, C. Bock and B. R. MacDougall, *P Roy Soc a-Math Phy*, 2015, **471**.
38. L. A. Burton, T. J. Whittles, D. Hesp, W. M. Linhart, J. M. Skelton, B. Hou, R. F. Webster, G. O'Dowd, C. Reece, D. Cherns, D. J. Fermin, T. D. Veal, V. R. Dhanak and A. Walsh, *J Mater Chem A*, 2016, **4**, 1312-1318.
39. B. Hou, D. Parker, G. P. Kissling, J. A. Jones, D. Cherns and D. J. Fermin, *Journal of Physical Chemistry C*, 2013, **117**, 6814-6820.
40. S. B. Kulkarni, A. D. Jagadale, V. S. Kumbhar, R. N. Bulakhe, S. S. Joshi and C. D. Lokhande, *Int J Hydrogen Energ*, 2013, **38**, 4046-4053.
41. D. P. Dubal, R. Holze and P. Gomez-Romero, *Sci Rep-Uk*, 2014, **4**.
42. F. Kooli and W. Jones, *Inorg Chem*, 1995, **34**, 6237-&.
43. F. Kooli, W. Jones, V. Rives and M. A. Ulibarri, *Journal of Materials Science Letters*, 1997, **16**, 27-29.
44. J. L. Gunjakar, A. M. More, K. V. Gurav and C. D. Lokhande, *Applied Surface Science*, 2008, **254**, 5844-5848.
45. C. Barriga, W. Jones, P. Malet, V. Rives and M. A. Ulibarri, *Inorg Chem*, 1998, **37**, 1812-1820.
46. J. L. Gunjakar, Y. K. Jo, I. Y. Kim, J. M. Lee, S. B. Patil, J. C. Pyun and S. J. Hwang, *J Solid State Chem*, 2016, **240**, 115-121.
47. J. L. Gunjakar, I. Y. Kim and S. J. Hwang, *Eur J Inorg Chem*, 2015, DOI: 10.1002/ejic.201402480, 1198-1202.
48. R. A. Nyquist and R. O. Kagel, *Infrared spectra of inorganic compounds (3800-45cm^{-1})*, Academic Press, New York,, 1971.
49. K. Fan, H. Chen, Y. Ji, H. Huang, P. M. Claesson, Q. Daniel, B. Philippe, H. Rensmo, F. Li, Y. Luo and L. Sun, *Nat Commun*, 2016, **7**, 11981.
50. H. B. Li, M. H. Yu, F. X. Wang, P. Liu, Y. Liang, J. Xiao, C. X. Wang, Y. X. Tong and G. W. Yang, *Nat Commun*, 2013, **4**, 1894.
51. J. Yan, Z. J. Fan, W. Sun, G. Q. Ning, T. Wei, Q. Zhang, R. F. Zhang, L. J. Zhi and F. Wei, *Adv Funct Mater*, 2012, **22**, 2632-2641.
52. J. W. Lee, T. Ahn, D. Soundararajan, J. M. Ko and J. D. Kim, *Chemical Communications*, 2011, **47**, 6305-6307.
53. S. J. Wu, X. H. Yang, J. F. Hu, H. W. Ma, Z. G. Lin and C. W. Hu, *Crystengcomm*, 2015, **17**, 1625-1630.
54. G. Silversmit, D. Depla, H. Poelman, G. B. Marin and R. De Gryse, *J Electron Spectrosc*, 2004, **135**, 167-175.